JACS
JOURNAL OF THE AMERICAN CHEMICAL SOCIETY
pubs.acs.org/JACS
Article

Lithium-Directed Transformation of Amorphous Iridium (Oxy)hydroxides To Produce Active Water Oxidation Catalysts

Jonathan Ruiz Esquius, David J. Morgan, Gerardo Algara Siller, Diego Gianolio, Matteo Aramini, Leopold Lahn, Olga Kasian, Simon A. Kondrat, Robert Schlögl, Graham J. Hutchings, Rosa Arrigo, and Simon J. Freakley*

Cite This: J. Am. Chem. Soc. 2023, 145, 6398–6409

ABSTRACT: The oxygen evolution reaction (OER) is crucial to future energy systems based on water electrolysis. Iridium oxides are promising catalysts due to their resistance to corrosion under acidic and oxidizing conditions. Highly active iridium (oxy)-hydroxides prepared using alkali metal bases transform into low activity rutile IrO_2 at elevated temperatures (>350 °C) during catalyst/electrode preparation. Depending on the residual amount of alkali metals, we now show that this transformation can result in *either* rutile IrO_2 or nano-crystalline Li-intercalated IrO_x. While the transition to rutile results in poor activity, the Li-intercalated IrO_x has comparative activity and improved stability when compared to the highly active amorphous material despite being treated at 500 °C. This highly active nanocrystalline form of lithium iridate could be more resistant to industrial procedures to produce PEM membranes and provide a route to stabilize the high populations of redox active sites of amorphous iridium (oxy)hydroxides.

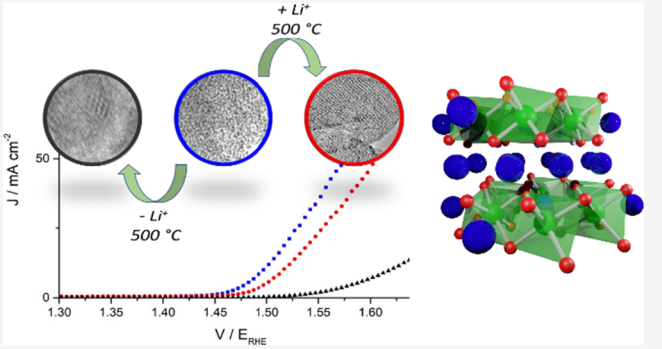

INTRODUCTION

Large-scale water electrolysis is key to the renewable chemical industry. Catalysts for the oxygen evolution reaction (OER) are often limited by instability under anodic potential in acidic electrolytes. Iridium oxides show promise under these conditions with comparatively limited corrosion compared to other catalysts such as RuO_2.[1−3] Various morphologies have been investigated to maximize activity and develop a fundamental understanding of the catalytic process. Metallic Ir nanoparticles have been studied under OER conditions and shown to form amorphous iridium(oxy)hydroxide ($Ir(O)_x(OH)_y$) shells which are the active form of the catalyst.[4,5] Nanoparticulate and thin film $Ir(O)_x(OH)_y$ outperforms crystalline rutile IrO_2 in terms of reduced overpotential (η)[6,7] which has been associated with higher structural flexibility,[8,9] coexistence of Ir(III)/Ir(IV),[10] and formation of electrophilic O^- sites under OER conditions.[11,12] Geiger et al. reported that annealing amorphous $Ir(O)_x(OH)_y$ films results in rutile IrO_2 (r-IrO_2) with reduced intrinsic activity, suggesting a fine balance between activity, stability, and structure of the catalysts.[10,13] X-ray absorption spectroscopy (XAS) has been extensively applied to study the electronic structure of catalysts *in situ* and suggests that Ir(IV) oxides form higher oxidation-state species under OER conditions.[14] This is supported by *operando* X-ray photoelectron spectroscopy (XPS) which revealed oxidized Ir species bound to electron-deficient oxygen.[11] The abundance of this oxyl species was linearly correlated with charge transfer suggesting formation via an oxidation/deprotonation of surface hydroxyl groups. Less crystalline $Ir(O)_x(OH)_y$ therefore enables an abundance of hydroxyl groups with increased structural flexibility that may easily coordinate water providing a path for O−O bond formation.

Gao et al. recently reported amorphous Li^+-doped IrO_x catalysts (η = 270 mV at 10 mA cm^{-2}) with high activity suggested to originate from flexible IrO_6 octahedra resulting from Li^+ incorporation not present in rutile IrO_2.[15] Willinger et al. studied amorphous $Ir(O)_x(OH)_y$ and similarly proposed flexible hollandite structural motifs as active sites.[16] Alkali-doped hollandite structures can be prepared under harsh conditions; Sun et al. synthesized $K_{0.25}IrO_2$ from $IrCl_3/K_2CO_3$ by annealing in air (600 °C, 6 h), and distorted IrO_6 octahedra were suggested to increase activity compared to stable rutile IrO_2.[17] We recently reported an amorphous IrO_x prepared via hydrothermal synthesis using Li_2CO_3 which showed high

Received: December 21, 2022
Published: March 9, 2023

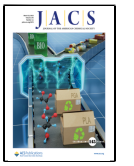

https://doi.org/10.1021/jacs.2c13567
J. Am. Chem. Soc. 2023, 145, 6398−6409

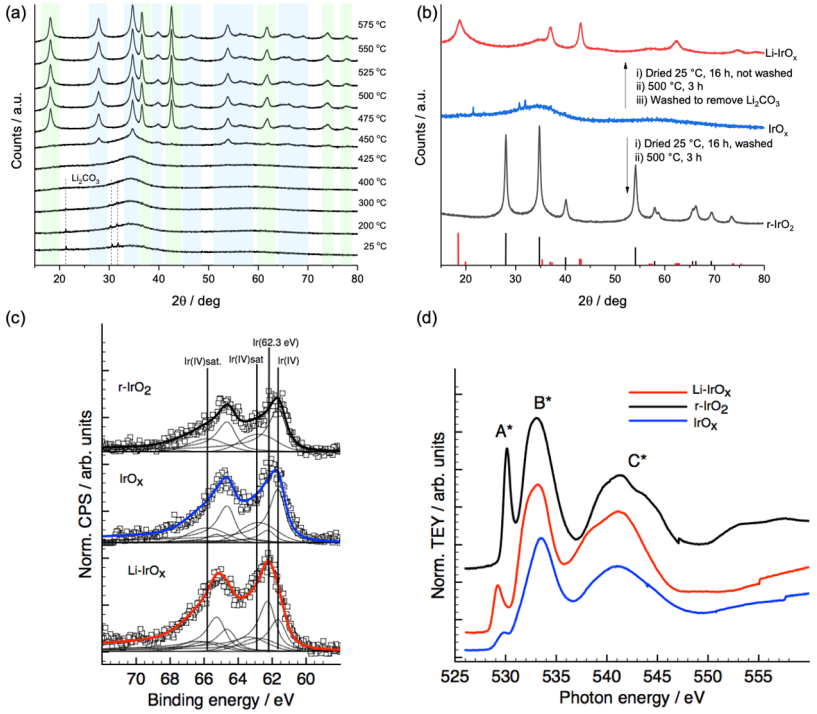

Figure 1. (a) *In situ* XRD pattern of as-prepared IrO_x-Li_2CO_3 under flowing air held for 5 min at each temperature before recording a diffraction pattern. Blue regions indicate rutile IrO_2 reflections and green regions represent Li-IrO_x. (b) XRD pattern of samples prepared by divergent preparation methods to control the residual Li_2CO_3. Black reference pattern rutile IrO_2 [ICSD-56009], red reference pattern β-Li_2IrO_3 [ICSD-246025]. (c) Fitted Ir 4f XPS spectra relative to the samples as indicated, measured in UHV and at an electron kinetic energy (KE) of 200 eV (left). (d) Total electron Yield (TEY) O K-edge NEXAFS spectra measured for IrO_x, Li-IrO_x, and r-IrO_2.

activity (η = 250 mV at 10 mA cm^{-2}) in comparison to a commercial hydrated IrO_x with a comparable Ir(III):Ir(IV) ratio, geometric surface area, and surface composition to the as-prepared material.[18] The higher intrinsic activity, when normalized to active electrochemical surface area (ECSA), suggested a possible promotional effect of residual alkali metal ions, in this case Li^+.

We now show that starting from amorphous $Ir(O)_x(OH)_y$, it is possible to form *either* rutile or Li-intercalated iridium oxide during thermal treatments depending on the level of residual Li^+. We find that this Li-intercalated iridium oxide shows comparable activity and increased stability compared to the amorphous material despite being treated at 500 °C—breaking the relationship between thermal treatment and deactivation of $Ir(O)_x(OH)_y$. Operando spectroscopy reveals mechanistic insights, and the stability of this material provides a framework for the design of improved OER anode systems.

RESULTS AND DISCUSSION

Structural Characterization of Iridium Oxides. The synthesis of iridium-oxyhydroxide (IrO_x) using Li_2CO_3 as a precipitating base was reported by our group as the basis for this study.[18] X-ray diffraction (XRD, Figure 1a) of the freshly prepared material shows broad features at 35°, typical of amorphous IrO_x and low-intensity diffraction of residual Li_2CO_3 [ICSD-16713]. *In situ* diffraction during heat treatments shows rutile IrO_2 [ICSD-56009] forms >425 °C consistent with the crystallization of amorphous IrO_x. The diffraction pattern of Li_2CO_3 is no longer observed, suggesting reaction or decomposition at lower-than-expected temperatures compared to the literature (~727 °C).[19] An additional diffraction pattern distinct to rutile IrO_2 developed above 450 °C, which is highlighted in green in Figure 1a. To probe the effect of residual Li_2CO_3, two further samples were prepared from the same IrO_x: (i) washed to remove all Li_2CO_3 (determined by the absence of the Li_2CO_3 diffraction pattern) and (ii) not washed to retain Li_2CO_3 after filtration and drying. Both were heated in static air (500 °C 3 h) and washed to remove residual Li_2CO_3. XRD (Figure 1b) shows distinctive phase transitions depending on the presence of Li_2CO_3. The Li^+-free IrO_x crystallizes into rutile IrO_2 (r-IrO_2) without any contaminant phase, confirmed by comparison to commercial IrO_2 (Figure S1). The sample with excess Li_2CO_3 crystallizes exclusively into a different phase (Li-IrO_x) with a crystallite size of ~11 nm; a small residual broad feature is consistent with some remaining amorphous material.

Lithium iridates are typically prepared by a high-temperature solid-state reaction between IrO_2/Ir black and Li_2CO_3.[20−22] Grimaud prepared β-Li_2IrO_3 by reacting Ir/IrO_2 and Li_2CO_3 at 1080 °C for 30 h.[23] Chan prepared similar Li-rich Li_nIrO_x by reacting IrO_2 and Li_2CO_3 at 950 °C for 2 days.[24] Both β-Li_2IrO_3 and α-Li_2IrO_3 contain layered structures of Ir-oxo sheets and intercalated Li^+ characterized by XRD between 18 and 20°. This can vary from ~18.2° for high Li^+ contents to 20° for low Li^+ or Li/H^+ intercalation corresponding to the IrO_6 sheet inter-planar distance.[25] The obtained new diffraction pattern largely aligns with the β-Li_2IrO_3 phase reported by O'Malley et al. who prepared samples by heating Li_2CO_3 and Ir metal at 750 °C 12 h before the increasing temperature to 1050 °C [ICSD-246025].[22] The nanocrystalline nature of our material means that low-intensity X-ray reflections of highly crystalline samples are likely below the detection limits. The observed principle reflection (18.3°)

https://doi.org/10.1021/jacs.2c13567
J. Am. Chem. Soc. 2023, 145, 6398−6409

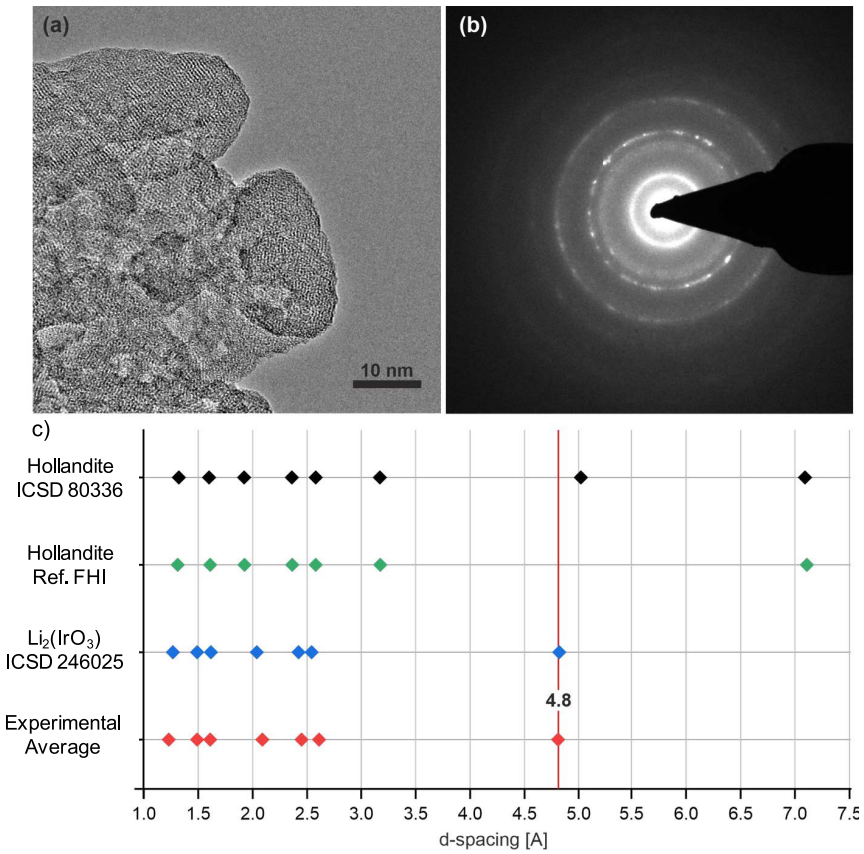

Figure 2. Electron microscopy characterization of Li-IrO_x. (a) High-resolution TEM image showing nanocrystalline domains. (b) Electron diffraction pattern of the heated sample corroborating that the sample is polycrystalline, (c) comparison between simulated hollandite and lithium iridate (β-Li_2IrO_3) as well as experimental hollandite (FHI)[16] and the average *d*-spacings taken from Li-IrO_x.

suggests that the layered Li-IrO_x has 0.48 nm spacing between Ir-oxo planes consistent with Li stoichiometry close to 2.[26]

XPS spectra of the Ir 4f levels (Figure 1c) were fitted considering an asymmetric main peak and shake-up satellite +1 eV to the main line.[10] A component (61.8 eV) consistent with crystalline rutile IrO_2 was observed for the synthesized r-IrO_2.[7] An additional component (62.3 eV) appears with associated satellite for the IrO_x material; this is the main component for the Li-IrO_x material and was reported for many amorphous iridium-oxyhydroxides *in situ* during OER.[6,27] *In situ* XPS studies suggest that Ir-oxide nanoparticles have surface oxidation states below Ir(IV) when terminal H_2O/OH species are chemisorbed with an Ir 4f binding energy of 62.3 eV. This suggests that the surfaces of both IrO_x and particularly Li-IrO_x are highly hydrated/hydroxylated rather than oxide-terminated.[28] Changes in the Ir oxidation state are mirrored by small binding energy shifts which are also sensitive to surface orientation/termination, making assignment of the formal surface oxidation state challenging, especially for a distribution of species. Surface oxygen species were investigated by O K-edge NEXAFS (Figure 1d) and characterized by two sharp resonances, *A** and *B**, assigned to O 1s excitation into hybridized O 2p-Ir 5d t_{2g} and e_g states, in addition to a higher energy resonance (*C**) from excitation into O 2p-Ir 6s-p hybridized states, respectively. A high ratio of *A**:*B** is characteristic of high M−O covalency and the degree of hybridization between O 2p and t_{2g} orbitals of the M−O bond.[29] The r-IrO_2 spectrum (Figure 1d) presents strong resonances at 530 and 533 eV in agreement with literature data for O^{2-} species.[6] A significant decrease in the *A** intensity for IrO_x indicates lower degree of hybridization, consistent with a higher ionic character. Moreover, this resonance appears split into two components with the additional component at 529 eV. Similarly, Li-IrO_x has a less intense *A** resonance, consistent with Li_2IrO_3 systems, and shifts to lower energy (~529 eV).[30] This pre-edge resonance was associated with electron hole states in hybridized Ir−O orbitals due to electrophilic oxygen species (oxyl species) which were suggested as active O species for nucleophilic attack by H_2O to form O−O bonds.[9] The presence of a hole in the oxygen valence band generates an intermediate valence ground state, with consequent appearance of extra features in the O K-edge spectra due to multielectron configuration in the excited final state; the apparent splitting of resonance *B** for IrO_x and Li-IrO_x could also be qualitatively explained by the presence of these species,[31] which are more pronounced for the Li-IrO_x system. Inspection of the resonance *C** region unveils peculiar structural characteristics of Li-IrO_x compared to that of r-IrO_2. Using a simple molecular orbital description, the broad resonance contains both the transition to the $3a_{1g}$ level (Ir 6s; O 2pσ) and the $4t_{1u}$ (Ir 6p; O 2pπ) level. In r-IrO_2, the decrease of the Ir−Ir distance in the direction perpendicular to the edges shared by the octahedra is associated with a degree of distortion of the Ir-O_6 octahedra.[32] This Ir−O distance is reflected in the position of the *C** resonances, whose peak maximum appears at approximately 539, 541, and 545 eV in r-IrO_2. A weaker interaction between Ir 6sp and O 2p (less dense structure) leads to a higher energy position of the

https://doi.org/10.1021/jacs.2c13567
J. Am. Chem. Soc. 2023, 145, 6398−6409

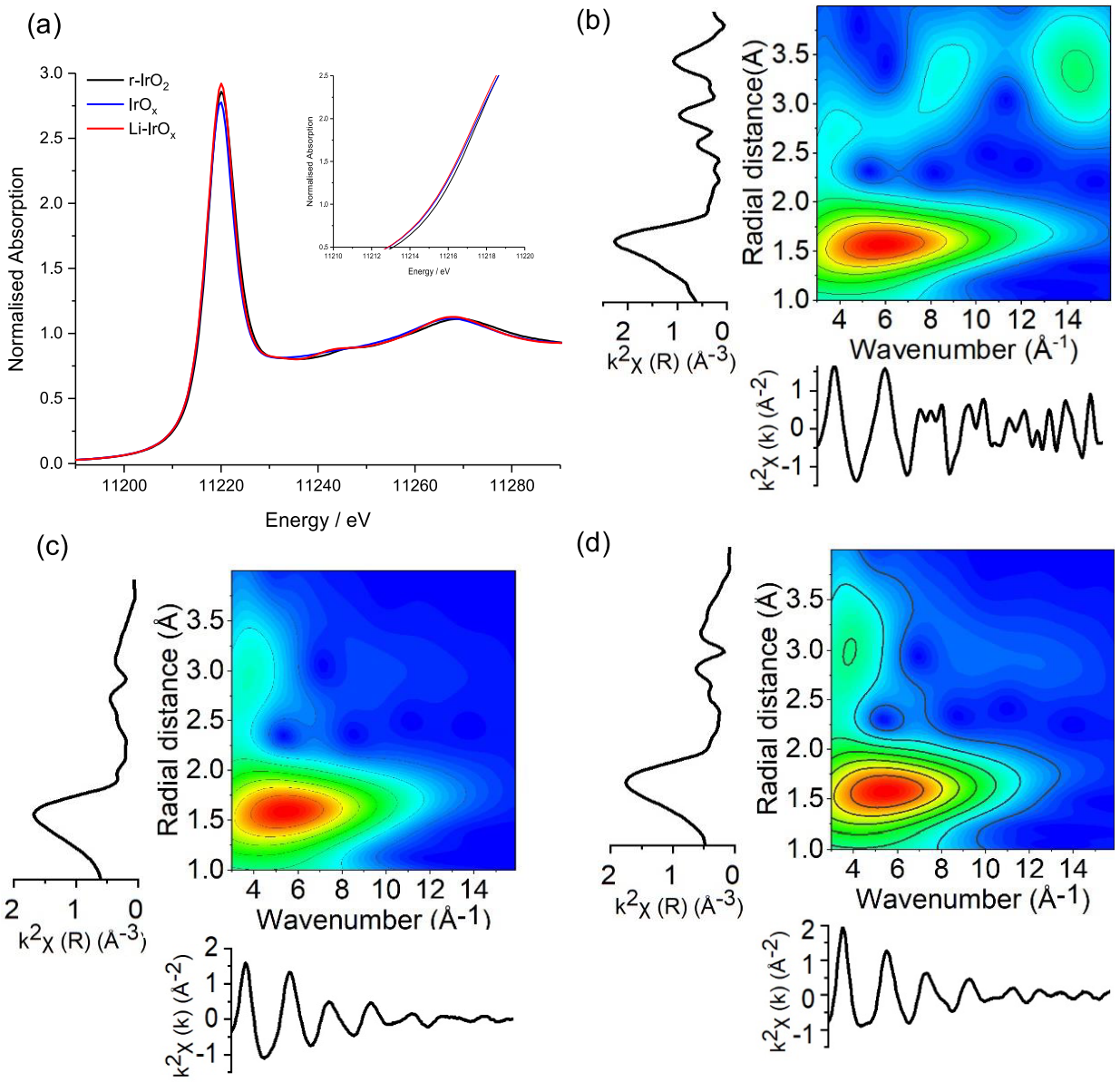

Figure 3. (a) Transmission Ir-L_3-edge XANES and wavelet EXAFS plots, with corresponding k^2 and FT magnitudes, for (b) r-IrO_2, (c) IrO_x, and (d) Li-IrO_x.

Table 1. EXAFS Model Fitting Parameters for Fresh r-IrO_2, IrO_x, Li-IrO_x, and $IrCl_3$ from Data Measured at the Ir-L_3-Edge

sample	scattering path	CN	R (Å)	$2\sigma^2$ (Å^2)	S_o^2	E_f (eV)	R_{factor} + (χ^2)
$IrCl_3$	Ir−Cl_1	6[a]	2.33(1)	0.003(1)	0.79	7.5(3)	0.018
r-IrO_2	Ir−O	6.1(1.6)	1.97(2)	0.002(10	0.79[a]	11.8(6)	0.04 (2830)
	Ir−Ir_1	3.0(1.5)	3.14(2)	0.004(2)			
	Ir−Ir_2	6.8(1.2)	3.55(1)	0.003(1)			
IrO_x	Ir−O	5.9(4)	2.013(4)	0.005(1)		12.5(5)	0.010 (2961)
	Ir−Ir	6[a]	3.14(2)	0.013(2)	0.79[a]		
	Ir−O_2	6[a]	3.64(2)	0.007 (2)			
Li-IrO_x	Ir−O	6.3(5)	2.000(6)	0.005(1)		12(1)	0.028 (2128)
	Ir−Ir_1	6[a]	3.09(2)	0.011(2)	0.79[a]		
	Ir−O_2	6[a]	3.62(3)	0.006(3)			

[a]Ir−Cl CN fixed at 6 to determine S_o^2 at a value of 0.79.

bonding orbitals, thus a lower energy position of the antibonding orbitals. In Li-IrO_x, the C^* resonances are found with maximum at 538 and 541 eV, indicating longer Ir−O bonds, whereas the distortion typical of rutile-type IrO_2 is no longer observed. On IrO_x, this resonance is broader, indicating a larger distribution of Ir−O bond lengths.

https://doi.org/10.1021/jacs.2c13567
J. Am. Chem. Soc. 2023, 145, 6398−6409

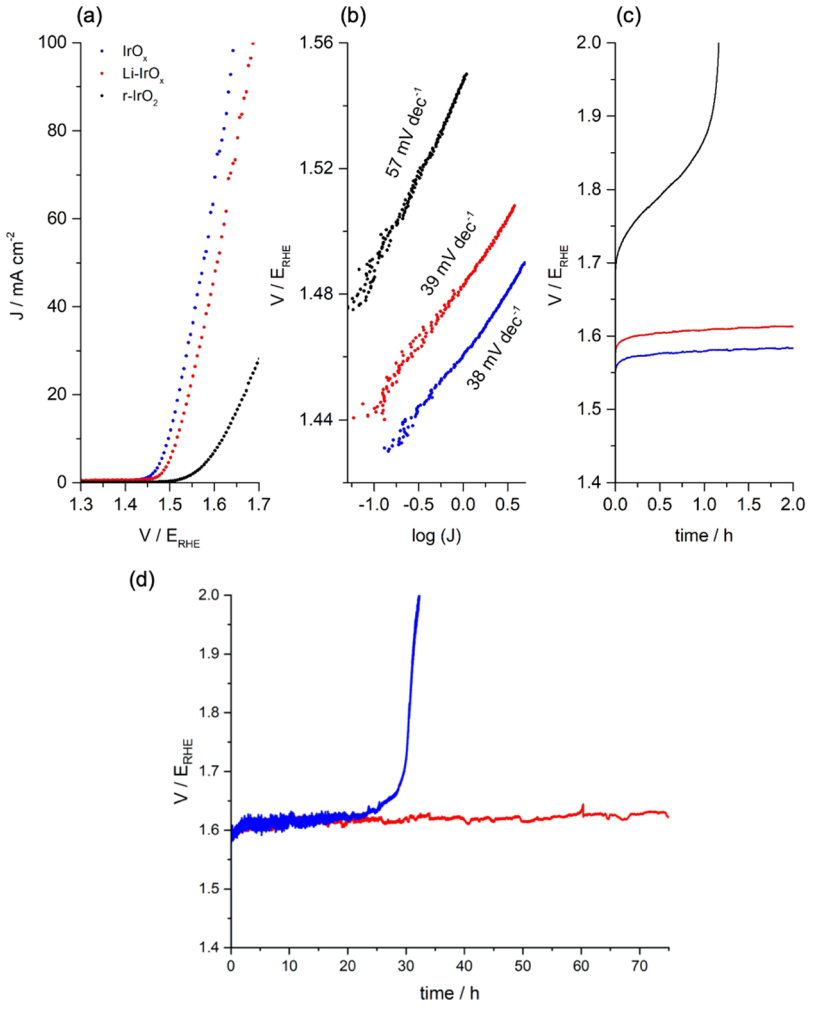

Figure 4. IrO$_x$, r-IrO$_2$, and Li-IrO$_x$ (a) activity (LSV, 1.2−1.7 V$_{RHE}$, 5 mV s^{-1}). (b) Tafel slope obtained from semi-steady-state conditions (LSV, 0.5 mV s^{-1}). (c) Long-term stability (CP, 10 mA cm^{-2}, 2 h) and (d) (CP, 10 mA cm^{-2}, 75 h) toward OER in a 0.1 M HClO$_4$ electrolyte.

High-resolution aberration-corrected transmission electron microscopy (TEM) shows that IrO$_x$ appears, as expected, amorphous (Figure S2), while Li-IrO$_x$ is polycrystalline with nanocrystalline domains (Figure 2). The Li-IrO$_x$ sample shows electron diffraction at *d*-spacing corresponding to those of lithium iridate (β-Li$_2$IrO$_3$) (ICSD-246025) consistent with XRD. The electron diffraction at multiple spots clearly shows that the material does not consist of rutile or alkali metal hollandite phases of IrO$_2$. The samples were studied by XAS at the Ir L$_3$-edge where interpretation of the absorption edge is complicated by a white line (WL) which is sensitive to symmetry, ligand environment, and oxidation state.[33] Figure 3a shows that r-IrO$_2$, IrO$_x$, and Li-IrO$_x$ have similar WL positions (11,219.8−11,220.0 eV) defined by the minimum in the second derivative. Comparison of Ir^0 (5d^7), IrCl$_3$ (5d^6), and IrO$_2$ (5d^5) (Figure S3) suggests a mixed valance Ir(IV)/Ir(III) species in the disordered IrO$_x$ material supported qualitatively by the reduced WL height as a direct probe of 5d occupancy.[18]

Extended X-ray absorption fine structure (EXAFS) spectra and wavelet transformations are shown in Figure 3; fitting parameters and suggested fits are shown in Tables 1 and S1 and Figures S4−5. r-IrO$_2$ was satisfactorily modeled with a first Ir−O$_6$ shell and second Ir−Ir shell.[14] The Ir−O path at 1.97(2) Å with a coordination number (CN) of 6.1(1.6) was consistent with Ir(IV) oxide species.[34] Ir−Ir$_1$ had a path length of 3.15(2) Å and a CN of 3.0(1.5) and Ir−Ir$_2$ at 3.55(1) Å and a CN of 6.8(1.2). Including Ir−O multiple scattering paths resulted in unrealistic $2\sigma^2$ values. The wavelet transformation shows a strong feature centered at low *R* (Δk 3−13 Å^{-1} and ΔR 1−2 Å) associated with the first Ir−O shell. The features at Δk 3−8 Å^{-1} and ΔR 2.5−3.0 Å are attributed to subsequent Ir−O shells and multiple scattering paths. The split feature at high Δk 9−16 Å^{-1} and ΔR 3.0−3.75 Å is due to the two heavy scattering Ir−Ir paths. Therefore, EXAFS analysis of r-IrO$_2$ confirms findings from XRD of an ordered rutile structured material. Contrasting IrO$_x$ and Li-IrO$_x$ with r-IrO$_2$ wavelet analysis, the first Ir−O$_6$ shell remains relatively consistent with a diminished contribution from the heavy scattering Ir−Ir paths. An additional feature (Δk 3−6 Å^{-1}, ΔR 2.75−3.5 Å) not seen in r-IrO$_2$ is observed for IrO$_x$ and with greater intensity in Li-IrO$_x$, indicating the presence of another light scatterer such as a different O species or Li. The data were fitted with a model of layered 2D edge-sharing [IrO$_6$], derived from the crystal structure of β-Li$_2$IrO$_3$ (ICSD-246025), including two simplified Ir−O shells (using a single averaged Ir−O distance vs the two distorted [IrO$_6$] environments within the β-Li$_2$IrO$_3$ crystal structure) and a single Ir−Ir path.[22] The CN of the first Ir−O path was floated, while all other path degeneracies were fixed. Given the challenges in accurately modeling Li scatterers, the fitting model used omitted these paths, although models

https://doi.org/10.1021/jacs.2c13567
J. Am. Chem. Soc. 2023, 145, 6398−6409

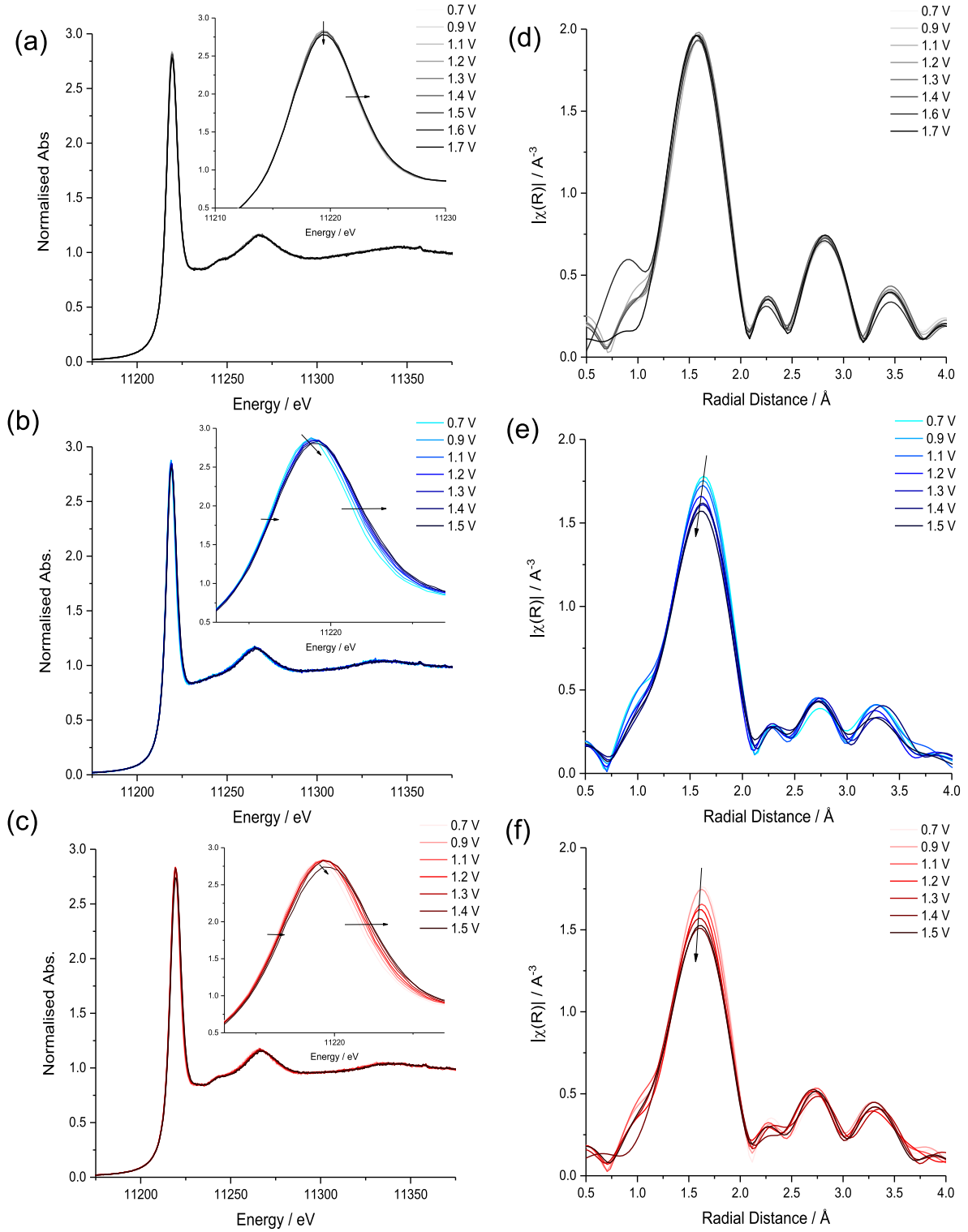

Figure 5. *In situ* normalized XANES spectra for (a) r-IrO_2, (b) IrO_x, and (c) Li-IrO_x recorded at different electrode potentials in 0.1 M $HClO_4$. Insets show an expansion of the absorption peak to highlight the change in position. Fourier-transformed Ir EXAFS spectra of (d) r-IrO_2, (e) IrO_x and (f) Li-IrO_x at given electrode potentials.

including the Ir−Li paths are included in the Supporting Information (Table S1). IrO_x is defined by a first shell [IrO_6] octahedron (Ir−O of 2.013(4) Å, CN 5.9(3)); elongated Ir−O bonds are consistent with increased structural disorder (higher $2\sigma^2$) relative to r-IrO_2 and reduced Ir species.[35] The second shell Ir−Ir (3.14(2) Å, CN = 6) and a high $2\sigma^2$ support layered edge-sharing Ir−O_6 octahedra with a longer Ir−Ir distance than crystalline β-Li_2IrO_3 (2.98 Å), suggesting increased structural disorder. No improvement in fitting was observed upon the inclusion of Li scattering paths, showing that EXAFS provides no evidence for the presence of ordered Li within the sample. A comparable fit was determined for Li-IrO_x, with a

https://doi.org/10.1021/jacs.2c13567
J. Am. Chem. Soc. 2023, 145, 6398−6409

sightly reduced Ir−O first shell distance of 2.000(6) Å and an Ir−Ir distance of 3.09(2) Å, coupled with a reduction in the latter paths $2\sigma^2$, indicating an increased structural order, further demonstrated by a visible XRD pattern. The inclusion of Li scattering paths (Table S1) did improve fitting results for Li-IrO_x, although given the challenge of fitting the extremely light Li scatters, the result is validated only by corroboration from the clear evidence of the layered structure by X-ray and electron diffraction. Therefore, EXAFS supports findings of the formation of a layered Li-IrO_x material at relatively mild temperatures compared to other reported synthetic procedures. The comparison of this structure to that of rutile IrO_2 based on the cited ISCD entries is shown in Figure S6.

Electrocatalytic Data. Lithium iridates prepared under harsh conditions (950 °C, 2 days) have been studied electrochemically to probe charging/discharging of Li^+ ions above 2 V_{RHE}.[24] The study suggests that at higher potentials, the charge capacity was predominantly attributed to oxidation of O^{2-} ions drawing similarity to OER mechanisms. Furthermore, McCalla et al. observed O−O peroxo dimers in similar layered oxide-type Li batteries.[36] Tarascon extended the study of lithium iridates suggesting that the open structure allows water to penetrate between the MO_2 planes rendering "bulk" $(O_2)^{n-}$ species active for the OER by Li/H exchange.[37] Pearce et al. synthesized highly crystalline β-Li_2IrO_3 prepared from IrO_2 and Li_2CO_3 at 1080 °C for 30 h and demonstrated that it was stable to dissolution under acidic conditions and under polarization is active towards the OER while undergoing Li/H^+ exchange.[25]

The OER activity of IrO_x, r-IrO_2, and Li-IrO_x in a 0.1 M $HClO_4$ electrolyte was assessed by LSV (1.2−1.7 V_{RHE}, 5 mV s^{-1}) without any pre-activation treatment (Figure 4a). r-IrO_2, Li-IrO_x, and IrO_x achieved 10 mA cm^{-2} at an overpotential (η) of 390, 290, and 270 mV, respectively. The synthesized Li-IrO_x shows comparable activity to both IrO_x and commercially available IrO_2·2HO (Premion Alfa Asear) in terms of the potential required to reach 10 mA cm^{-2} (IrO_x −1.50 V, Li-IrO_x −1.51 V, IrO_2·H_2O −1.52 V—despite being thermally treated at 500 °C. Similar electrochemically active surface areas (ECSAs) were obtained for IrO_x (0.005 mF cm^2) and Li-IrO_x (0.006 mF cm^2) by normalizing the double-layer capacitance by the specific capacitance (Figure S7).[38] Tafel slopes (Figure 4b) for IrO_x (38 mV dec^{-1}) and Li-IrO_x (39 mV dec^{-1}) agreed with previous results reported for (oxy)hydroxides (ca. 40 mV dec^{-1}), which suggests a similar dependence of the reaction rate on potential.[15,39,40] However, a higher Tafel slope for r-IrO_2 (57 mV dec^{-1}) was in agreement with literature (ca. 60 mV dec^{-1}) and slower kinetics.[41,42] Comparable onset potentials between Li-IrO_x and IrO_x, similar ECSA and Tafel slopes indicate that the layered nanocrystalline Li-IrO_x has similar electrochemical properties to the amorphous IrO_x and outperforms r-IrO_2 which has been thermally treated at the same temperature, 500 °C, giving a clear indication that residual Li^+ can prevent thermal deactivation of amorphous IrO_x.

Cyclic voltammetry (CV) of IrO_x (Figure S8) showed characteristic Ir^{3+}/Ir^{4+} and Ir^{4+}/Ir^{5+} redox events at 0.9 and 1.2 V_{RHE} indicating facile redox processes at the surface and were also observed for Li-IrO_x at the same potentials.[25,43] No characteristic features were observed for r-IrO_2, suggesting that it is much less redox active and hence likely a poor catalyst for the OER.[44] Catalyst stability was assessed through chronopotentiometry (10 mA cm^{-2}) in Figure 4c; IrO_x and Li-IrO_x showed good stability over the 2 h test with degradation rates of 5.9 and 6.9 mV h^{-1}, respectively. However, r-IrO_2 showed complete deactivation within the first hour in agreement with previous reports.[18] Longer term stability testing of IrO_x and Li-IrO_x at 10 mA cm^{-2} was conducted for 75 h (Figure 4d). During the first 25 h, IrO_x and Li-IrO_x showed similar performance with potentials ∼1.61 V_{RHE}. The IrO_x catalyst then rapidly degraded after 25 h; in contrast, Li-IrO_x showed stable performance during at least 75 h with a degradation rate stabilizing at 0.3 mV h^{-1}. Stability testing at higher current density (100 mA cm^{-2}) also shows enhanced stability in Li-IrO_x with stable operation for 8 h when compared to only 4 h for IrO_x (Figure S9). Under high current density deactivation might not be necessarily related solely to catalyst corrosion but also to mechanical processes such as catalyst detachment induced by the high rate of bubble formation. Prolonged stability tests at high current densities are more reliable for freestanding or self-supported catalysts. Nevertheless, our catalytic results suggest that nanocrystalline iridate structures are comparative OER catalysts to iridium(oxy)hydroxides despite being exposed to temperatures which would normally deactivate amorphous systems. In this case, thermal treatment resulted in enhanced durability, which allows the desired balance between relatively high activity and long-term stability.

Operando Spectroscopy. Czioska et al. recently conducted *operando* XAS of IrO_2 and proposed that WL position is related to changes in surface speciation without modification of the IrO_2 structure. Nattino et al. also reported WL shifts toward higher energies on deprotonation of surface hydroxyls, while WL height changes are caused by changes in d-band occupancy or emerging spectral features.[14,45] *Operando* XAS spectra at 100 mV potential steps between 0.7 and 1.6 V were recorded for the three samples (Figure 5a−c). In contrast to Czisoka, we did not observe a WL height reduction and shift on applying "high" OER potentials (1.7 V_{RHE}), proposed to result from increased Ir−Ir interactions through O-vacancy formation. Under applied potential, the WL of r-IrO_2 remained largely unchanged, suggesting a minimal change in the Ir coordination. Due to reduced data quality, even simplified second shell structural models gave large errors meaning that structural information concerning the second coordination shell was limited.[40,46] We applied a first shell Ir−O_6 model by initially allowing CN, R, and $2\sigma^2$ of Ir−O to be floated and fixing the structural disorder factor at this value for subsequent fittings to avoid strong correlations between CN and structural disorder. Upon increasing potential from 0.9 to 1.7 V, Ir−O_1 remained relatively consistent at 1.96−1.97 ± 0.01 Å as did the Ir−O coordination, 6.5 ± 0.4 at 0.9 V to 6.6 ± 0.8 at 1.7 V (Table S2) confirming the relative stability and lack of structural evolution.

Upon analysis of IrO_x with increasing potential (0.7−1.5 V) (Figure 5c,d), the WL position increased from 11,218.8 to 11,219.2 eV, suggesting more facile oxidation (deprotonation) or changes in surface Ir−O speciation. The FWHM increases from 7.3 to 8.1 eV giving asymmetrical broadening of the WL. The simplified fitting model (Table S3) suggests Ir−O_1 of 2.02 ± 0.02 Å at 0.9 V and 2.00 ± 0.01 Å at 1.5 V with CN changing from 5.6 ± 1.1 at 0.9 V and 4.9 ± 0.5 at 1.5 V. Li-IrO_x (Figure 5e,f) shows the WL shift from 11,219.1 to 11,219.3 eV consistent with changes in surface speciation suggested by Czisoka et al.[45] Above 1.2 V, the FWHM broadens significantly from 7.8 to 8.4 eV with the WL height decreasing from 2.85 at 1.2 V to 2.74 at 1.5 V, suggesting the

https://doi.org/10.1021/jacs.2c13567
J. Am. Chem. Soc. 2023, 145, 6398−6409

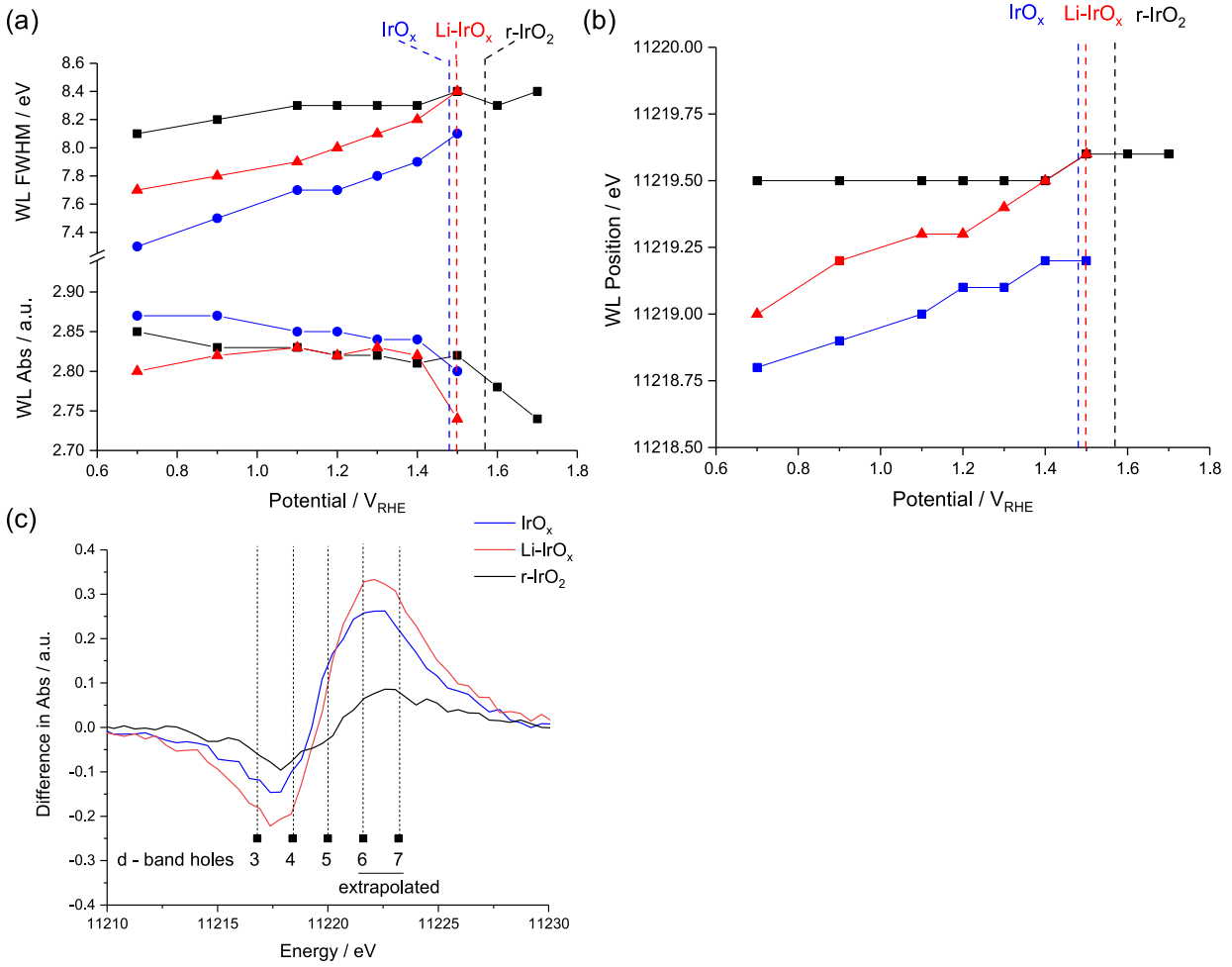

Figure 6. Numerical analysis of the *in situ* XANES spectra. (a) White line (WL) absorbance and FWHM, (b) WL position, and (c) difference in XANES spectra between the lowest and highest potentials studied.

development of a higher energy spectral feature and changes in the underlying structure. Similar to the IrO_x material, fitting suggests Ir−O_1 of 2.02 ± 0.01 Å at 0.9 V and 2.00 ± 0.01 Å at 1.5 V with a significantly reduced Ir−O_1 CN of 5.7 ± 1.1 at 0.9 V and 5.0 ± 0.6 at 1.5 V (Table S4). The fitting suggests that under the applied potential, IrO_x and Li-IrO_x behave similarly and form a significant number of O-vacancies. In the case of r-IrO_2 and IrO_x, these changes were recoverable on the cathodic sweeps (Figure S10), however, not fully for Li-IrO_x despite the stable OER activity. EXAFS fitting suggests changes in the Ir−O environment, which could be consistent with the exchange of Li^+/H^+ and protonation/deprotonation of both the surface and interplane Ir−O species.[25]

Combining these observations, samples with higher binding energy Ir species measured by XPS (IrO_x and Li-IrO_x) or oxygen species carrying an electron hole as determined by O K-edge XANES undergo WL shifts with increasing potential (Figure 6a,b), suggesting more redox active surfaces compared to r-IrO_2. The highly active OER catalysts show WL asymmetric broadening to higher energy (by 0.3−0.9 eV) over the potential range which could suggest that FWHM broadening and decrease in WL intensity are not a result of the same processes as correlations between the WL position - intensity and FWHM - intensity were poor across all samples (R^2 = <0.45) (Figure S11). This conclusion is also supported by the results of our ab initio simulations reported in the Supporting Information (Figure S12). A significant reduction in WL height is seen at the respective OER onset (dotted lines in I−V plots, Figure 6a)—this could represent a change in the d-band occupancy associated with O-vacancy formation without significant changes in Ir−Ir coordination. A good correlation (R^2 = 0.93) is seen between the WL position and FWHM broadening meaning that deconvolution of a surface oxidation process (WL position) and evolution of higher energy spectral features (FWHM) is challenging. The shift and broadening could be a result of the development of oxidized Ir−O moieties consistent with many proposed OER mechanisms.

Difference spectra (Figure 6c) show asymmetry between the lowest and highest potential measurements. Superimposed are the WL positions derived from Figure S3. The r-IrO_2 sample shows the smallest difference—implying that the Ir(IV) species measured by XPS and XAS are not redox active species in the bulk of the sample. IrO_x and Li-IrO_x show greater differences, suggesting that increased amounts of redox active Ir exist at the electrode/electrolyte interface. In the OER region, all samples have a significant increase in intensity at higher energies associated with asymmetric FWHM broadening, extrapolating beyond the standards recorded in Figure S3; it is clear that all samples show the formation of a similar feature or combination of features with an observed maximum intensity of ∼11,222.6 eV. We assign this to a more electron-deficient Ir−O species

https://doi.org/10.1021/jacs.2c13567
J. Am. Chem. Soc. 2023, 145, 6398−6409

than the Ir(IV)−O in rutile-type IrO_2 or the Ir(IV)−O−Li in Li-IrO_x or IrO_x. This spectral transformation is consistent with the formation of metastable Ir(V)/μ_1-oxyl species proposed as OER intermediate species.[28] High OER activity and more pronounced structural changes for IrO_x and Li-IrO_x correlate well with the enhanced redox dynamics observed by CV. A more reactive surface and higher OER activity can be correlated to the initial Ir speciation in these systems, with the higher binding energy component more susceptible to undergo redox dynamics leading to the evolution of O_2.[47−51] We can conclude that all three materials undergo similar evolution under polarization but to different degrees with an OER mechanism involving the formation of Ir(V)/μ_1-oxyl species as well as the generation of oxygen vacancies (shift of the L_3-edge to a higher energy in the X-ray absorption near-edge structure (XANES) spectrum and decrease of its intensity in the experimental XANES data and in the simulated XANES in Figure S10). Similar to previous work, we postulate that these Ir(V)/μ_1-oxyl species are formed under anodic potentials via deprotonation and oxidation of the surface Ir−OH of r-IrO_2 or Ir−O−Li species on Li-IrO_x and IrO_x. Due to their electrophilic character, Ir(V)/μ_1-oxyl species are susceptible to undergo nucleophilic attack by neighboring OH species forming the intermediate O−O bond that results in the evolution of oxygen and formation of the vacancies. We suggest that the exceptional stability of the layered Li-IrO_x system might be explained by the fact that this transformation becomes anisotropic for a layered structure, which retains a stable backbone structure of Ir-oxo layers, whereas oxyl species are formed from the longer Ir−O bonds seen in these systems in the O K-edge NEXAFS spectra in Figure 1d. The presence of longer Ir−O bonds, possibly due to the polarizing effect of Li^+ species, could lead to these being preferentially involved in the O−O bond formation. It is possible that these oxygen ligands are oriented perpendicularly to the layers and located within the interlayer space where the oxygen turn over preferentially takes place. In contrast, in the case of IrO_x, this transformation involves both axial and equatorial oxygen species, ultimately leading to a disruption of the structure and dissolution of Ir species upon water ligation causing a deterioration of the performance.

Thermal Processing of Li-IrO_x. Li-IrO_x which has been thermally treated at 500 °C retains high activity comparable to IrO_x which is dried at room temperature to prevent conversion to rutile. Due to the sensitivity toward drying temperatures, extreme care must be taken in the preparation of electrodes, which becomes challenging at scale when dry weight is used to estimate Ir loadings requiring elevated drying temperatures (>100 °C).[52,53] Figure 7a records the LSV of IrO_x electrodes dried at room temperature and 130 °C for 2 h. The results suggest a deactivation of IrO_x with increased drying temperature with a change of 60 mV needed to achieve 50 mA cm^{-2}. In contrast, Li-IrO_x which has been thermally treated at 500 °C shows a change of just 13 mV at comparable current densities suggesting a high stability to harsher electrode preparation conditions (Figure 7b).

CONCLUSIONS

Many studies utilize alkali metals as precipitating agents for the synthesis of iridium oxides used in electrocatalytic reactions. This study shows for the first time that the residual Li^+ can supress the formation of rutile IrO_2 on the thermal treatment of amorphous oxides and hence deactivation for the OER and instead direct the transformation to produce a nanocrystalline layered Li-iridate at relatively mild conditions. This iridate shows comparable activity to amorphous iridium oxyhydroxides despite being treated at 500 °C and enhanced stability over extended reaction times. The dynamics of the L_3-edge spectroscopic features of this electrocatalyst under the oxygen evolution reaction are like those observed for the rutile IrO_2 and the amorphous IrO_x indicating similar structural dynamics and thus reaction mechanism. The incorporation of structural alkali metal dopants into layered oxides provides a route to not only stabilize high activity materials but also to controllably tune the electronic properties of metal oxide surfaces. We show herein that a layered structure allowed us to realize orthogonality between activity and stability, the latter being a major bottleneck in the design of OER active electrocatalysts.

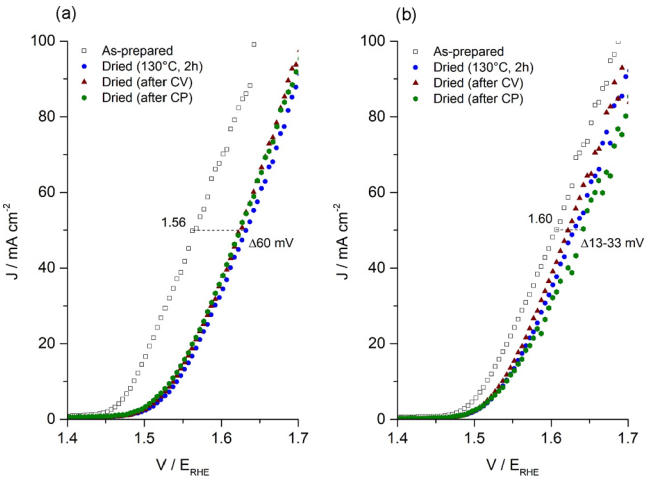

Figure 7. Effect of electrode drying (130 °C, 2 h) on the OER activity (LSV, 1.2−1.7 V_{RHE}, 5 mV s^{-1}) compared to as-prepared electrodes for (a) IrO_x and (b) Li-IrO_x.

EXPERIMENTAL SECTION

Synthesis of Ir-Based Materials. Amorphous iridium oxyhydroxide (IrO_x) was prepared following a precipitation method reported previously.[18] 299 mg of $IrCl_3$ hydrate (1 mmol) and 591 mg of Li_2CO_3 (8 mmol) were dissolved in 10 mL of deionized water and stirred for 16 h at 25 °C. A further 10 mL of deionized water was added, followed by heating to reflux for 3 h. The mixture was allowed to cool to room temperature. The formed precipitate was recovered by filtration and washed with 1 L of cold water and 1 L of hot water. The solid was dried in an open vessel at 25 °C for 16 h. Rutile IrO_2 (r-IrO_2) was prepared by annealing IrO_x in static air (500 °C, 10 °C min^{-1}, 3 h) . Lithium-doped IrO_x (Li-IrO_x) was synthesized as follows: 299 mg of $IrCl_3$ hydrate (1 mmol) and 591 mg of Li_2CO_3 (8 mmol) were dissolved in 10 mL of deionized water and stirred for 16 h at 25 °C. A further 10 mL of deionized water was added, followed by heating to reflux for 3 h. After cooling to room temperature, the precipitate was recovered by filtration without any washing step, dried in an open vessel (25 °C, 16 h), and annealed in static air (500 °C, 10 °C min^{-1}, 3 h). Excess Li_2CO_3 and Cl contamination were removed by washing with 1 L of hot and 1 L of cold deionized water. Finally, the material was dried in an open vessel at 25 °C for 16 h.

Catalyst Characterization. Powder XRD was performed on a (θ−θ) PANalyticalX'pert Pro powder diffractometer fitted with a position-sensitive detector using a Cu Kα radiation source (40 keV, 40 mA). An *in situ* Anton Parr XRK900 cell was used to monitor the crystallization while heating to 575 °C under static air. At each temperature step, the heating ramp (10 °C min^{-1}) was paused and the sample was held at that temperature, while a diffraction pattern was measured between 15 and 80° 2θ.

https://doi.org/10.1021/jacs.2c13567
J. Am. Chem. Soc. 2023, 145, 6398−6409

Samples were deposited dry on the TEM grids and characterized in an aberration-corrected Titan 80−300 operated at 200 kV.

Ir 4f XPS and O K-edge measurements were performed on the pelletized samples at the AP-XPS end station of the ISISS beamline (BESSY II) at 10^{-7} mbar base pressure. Ir 4f spectra were recorded by collecting photoemitted electron with a kinetic energy of 200 eV at a pass energy of the electron analyzer set to 20 eV. The energy of the spectra was calibrated against the Fermi level measured at the same excitation energy. The spectra were fitted using the fitting developed in refs 6, 7, 53, 10 after Shirley background subtraction. The O K-edge NEXAFS spectra were collected in total electron yield mode by detecting the sample drain current with a current amplifier. The relative energy calibration of the spectra was checked using features in the drain current of the last refocusing mirror of the beamline, then setting the pre-edge feature of the rutile type sample to 530 eV, and shifting the other spectra for the same amount. Spectra were normalized to the maximum intensity at 546 eV, after linear background subtraction.

XAS spectra were recorded in fluorescence mode at the Ir L_3 edge, at the B18 beamline of the Diamond Light Source, at Harwell, U.K. Prior to ex situ and *in situ* XAS analysis, 56 μL of catalyst ink dispersion (5 mg catalyst in 1.23 mL of water, 1.23 mL of ethanol, and 40 μL of Nafion solution) was drop-cast on a 5 mm × 5 mm square of carbon cloth (Sigracet 39 AA, 50 g m^{-2}, Fuel Cell Store) to obtain a catalyst loading of 150 mg_{cat} cm^{-2}. Five scans were recorded, and the averaged signal was used for data analysis. The measurements were performed using a QEXAFS setup with a fast-scanning Si (111) double crystal monochromator. For the *in situ* measurements, the time resolution of the data acquisition was ∼60 s/spectrum. XANES and EXAFS data were interpreted using IFEFFIT with Demeter software package (Athena and Artemis) using structural models available from ICDD as cited in the text. *In situ* XAS measurements were carried out using a sealed cell described previously in literature filled with a 0.1 M $HClO_4$ electrolyte. A Pt wire and a Ag/AgCl electrode were used as counter and reference electrodes, respectively.[54]

The density functional theory (DFT) calculations presented in Figure S11 were performed using the plane-wave pseudopotential DFT method available within the code CASTEP. Generalized-gradient approximation for the exchange-correlation energy was selected in the form of the solid-state revised PBE functional. Norm-conserving pseudopotentials used for PBE calculations were generated self consistently. A kinetic energy cutoff of 1150 eV for the wave function and a (10 × 10 × 10) Monkhorst-Pack *k*-point grid were determined as parameters for converged calculations. After introducing the localized structural defect (either vacancy of additional, bound oxygen), the structures have been relaxed to a tolerance energy of 1×10^{-6} eV/atom and forces of 2×10^{-2} eV/atom. A slightly extended k-point grid (12 × 12 × 12) was used for the simulation of spectroscopy results. XANES spectra were computed by extracting the matrix elements for electronic inter-band transitions from the ground-state DFT perturbed with the inclusion of the local effects of 2p core-hole, as available in the code. A transition broadening, because of instrumental resolution (Gaussian) and core-lifetime (Lorentzian) effects, was applied with values of 0.2 and 5 eV FWHM, respectively.

Catalytic Activity toward the Oxygen Evolution Reaction. Catalysts were tested on a three-electrode setup in a 0.1 M $HClO_4$ electrolyte. A coiled Pt wire (127 μm diameter, 99.99%, Sigma-Aldrich) was used as the counter electrode, a glassy carbon electrode with PEEK isolation (10 mm OD, 5 mm ID, IJ Cambria Scientific Ltd.) was used as the working electrode, and a calomel electrode ($[Cl^-/Hg_2Cl_2/Hg/Pt]$, IJ Cambria Scientific Ltd., model CHI-150) was used as the reference electrode. To prepare the catalyst ink, 5 mg of catalyst, 1.23 mL of water, 1.23 mL of ethanol, and 40 μL of Nafion solution were sonicated for 30 min to ensure a complete dispersion. 10 μL of the catalyst ink was drop-cast onto the working electrode and dried in the open at 25 °C for 16 h. The catalyst activity toward OER was measured by linear sweep voltammetry (LSV, 1.2 to 1.7 V_{RHE} at 5 mV s^{-1}). Catalyst stability was assessed by CV (0.7 to 1.7 V_{RHE}, 50 mV s^{-1}, 50 cycles) and chronopotentiometry (CP, 2 h at 10 mA cm^{-2}). Stability testing on the longer timescale was conducted by chronopotentiometry at 10 mA cm^{-2} for 75 h using an H-cell setup. The double-layer capacitance (C_{DL}) was obtained from CVs in the 0.4−0.5 V_{RHE} region at different scan rates (2, 5, 10, 20, 40, and 80 mV s^{-1}). The ECSA was obtained by dividing the C_{DL} by the specific capacitance in acid media ($C_{s,ac}$ = 0.035 mF cm^{-2}). Tafel slopes were derived from semi-steady-state conditions obtained from LSV measurements performed at low overpotential (1.43−1.56 V_{RHE}, 0.5 mV s^{-1}). Reported values are expressed against the reversible hydrogen electrode (RHE).

■ ASSOCIATED CONTENT

Supporting Information

The Supporting Information is available free of charge at https://pubs.acs.org/doi/10.1021/jacs.2c13567.

XRD, electron microscopy, X-ray absorption, EXAFS fittings, and electrochemistry (PDF)

■ AUTHOR INFORMATION

Corresponding Author

Simon J. Freakley − *Department of Chemistry, University of Bath, Bath BA2 2AY, U.K.;* orcid.org/0000-0002-6395-6646; Email: s.freakley@bath.ac.uk

Authors

Jonathan Ruiz Esquius − *Max Planck-Cardiff Centre on the Fundamentals of Heterogeneous Catalysis FUNCAT, Cardiff Catalysis Institute, School of Chemistry, Cardiff University, Cardiff CF10 3AT, U.K.; International Iberian Nanotechnology Laboratory, Braga 4715-330, Portugal;* orcid.org/0000-0002-3809-5389

David J. Morgan − *Max Planck-Cardiff Centre on the Fundamentals of Heterogeneous Catalysis FUNCAT, Cardiff Catalysis Institute, School of Chemistry, Cardiff University, Cardiff CF10 3AT, U.K.;* orcid.org/0000-0002-6571-5731

Gerardo Algara Siller − *Department of Inorganic Chemistry, Fritz Haber-Institut der Max-Planck-Gesellschaft, 14195 Berlin, Germany;* Present Address: Now at AG Strukturforschung/Elektronenmikroskopie, Institut für Physik, Humboldt-Universität zu Berlin, Newtonstraße 15 12489 Berlin, Germany (G.A.S.)

Diego Gianolio − *Diamond Light Source Ltd, Didcot OX11 0DE, U.K.;* orcid.org/0000-0002-0708-4492

Matteo Aramini − *Diamond Light Source Ltd, Didcot OX11 0DE, U.K.*

Leopold Lahn − *Helmholtz Institut Erlangen-Nürnberg, Helmholtz-Zentrum Berlin GmbH, 91058 Erlangen, Germany; Department of Materials Science and Engineering, Friedrich-Alexander-Universität Erlangen-Nürnberg, 91058 Erlangen, Germany*

Olga Kasian − *Helmholtz Institut Erlangen-Nürnberg, Helmholtz-Zentrum Berlin GmbH, 91058 Erlangen, Germany; Department of Materials Science and Engineering, Friedrich-Alexander-Universität Erlangen-Nürnberg, 91058 Erlangen, Germany;* orcid.org/0000-0001-6315-0637

Simon A. Kondrat − *Department of Chemistry, Loughborough University, Loughborough, Leicestershire LE11 3TU, U.K.;* orcid.org/0000-0003-4972-693X

Robert Schlögl − *Department of Inorganic Chemistry, Fritz Haber-Institut der Max-Planck-Gesellschaft, 14195 Berlin, Germany; Department of Heterogeneous Reactions, Max*

Planck Institute for Chemical Energy Conversion, 45470 Mulheim an der Ruhr, Germany

Graham J. Hutchings − *Max Planck-Cardiff Centre on the Fundamentals of Heterogeneous Catalysis FUNCAT, Cardiff Catalysis Institute, School of Chemistry, Cardiff University, Cardiff CF10 3AT, U.K.;* orcid.org/0000-0001-8885-1560

Rosa Arrigo − *School of Science, Engineering and Environment, University of Salford, Manchester M5 4WT, U.K.*

Complete contact information is available at: https://pubs.acs.org/10.1021/jacs.2c13567

Notes

The authors declare no competing financial interest.

■ ACKNOWLEDGMENTS

We would like to show our gratitude to the MaxNet Energy research consortium for financial support. G.J.H. acknowledges the Max Planck Centre for Fundamental Heterogeneous Catalysis (FUNCAT) for financial support. We acknowledge Diamond Light Source for time on Beamline B18 under Proposal SP18701-1 and the UK Catalysis Hub for allowing access through Bulk Allocation Group SP15151-10. Alex Mayer is thanked for processing the acquired data into wavelet plots. O.K. acknowledges support from the German Federal Ministry of Education and Research in the framework of the project CatLab (03EW0015A/B).

■ REFERENCES

(1) Naito, T.; Shinagawa, T.; Nishimoto, T.; Takanabe, K. Recent advances in understanding oxygen evolution reaction mechanisms over iridium oxide. *Inorg. Chem. Front.* **2021**, *8*, 2900−2917.

(2) Jang, H.; Lee, J. Iridium oxide fabrication and application: A review. *J. Energy Chem.* **2020**, *46*, 152−172.

(3) Wang, C.; et al. Iridium-Based Catalysts for Solid Polymer Electrolyte Electrocatalytic Water Splitting. *ChemSusChem* **2019**, *12*, 1576−1590.

(4) Bizzotto, F.; Arenz, M.; Quinson, J. Surfactant-free Ir nanoparticles synthesized in ethanol: Catalysts for the oxygen evolution reaction. *Mater. Lett.* **2022**, *308*, No. 131209.

(5) Cherevko, S.; Geiger, S.; Kasian, O.; Mingers, A.; Mayrhofer, K. J. J. Oxygen evolution activity and stability of iridium in acidic media. Part 2. − Electrochemically grown hydrous iridium oxide. *J. Electroanal. Chem.* **2016**, *774*, 102−110.

(6) Pfeifer, V.; et al. Reactive oxygen species in iridium-based OER catalysts. *Chem. Sci.* **2016**, *7*, 6791−6795.

(7) Pfeifer, V.; et al. The electronic structure of iridium oxide electrodes active in water splitting. *Phys. Chem. Chem. Phys.* **2016**, *18*, 2292−2296.

(8) Huang, F.; Jin, Y.; Wen, L. Investigations of the Hydration Effects on Cyclic Thermo-Oxidized Ir/IrO_x Electrode. *J. Electrochem. Soc.* **2015**, *162*, 337−343.

(9) Karimi, F.; Bazylak, A.; Peppley, B. A. Effect of Calcination Temperature on the Morphological and Electrochemical Characteristics of Supported Iridium Hydroxyoxide Electrocatalysts for the PEM Electrolyzer Anode. *J. Electrochem. Soc.* **2017**, *164*, F464−F474.

(10) Minguzzi, A.; Lugaresi, O.; Achilli, E.; Locatelli, C.; Vertova, A.; Ghigna, P.; Rondinini, S. Observing the oxidation state turnover in heterogeneous iridium-based water oxidation catalysts. *Chem. Sci.* **2014**, *5*, 3591−3597.

(11) Massué, C.; et al. Reactive Electrophilic OI−Species Evidenced in High-Performance Iridium Oxohydroxide Water Oxidation Electrocatalysts. *ChemSusChem* **2017**, *10*, 4786−4798.

(12) Nong, H. N.; et al. Key role of chemistry versus bias in electrocatalytic oxygen evolution. *Nature* **2020**, *587*, 408−413.

(13) Geiger, S.; Kasian, O.; Shrestha, B. R.; Mingers, A. M.; Mayrhofer, K. J. J.; Cherevko, S. Activity and Stability of Electrochemically and Thermally Treated Iridium for the Oxygen Evolution Reaction. *J. Electrochem. Soc.* **2016**, *163*, F3132−F3138.

(14) Reksten, A. H.; Russell, A. E.; Richardson, P. W.; Thompson, S. J.; Mathisen, K.; Seland, F.; Sunde, S. An in situ XAS study of high surface-area IrO_2 produced by the polymeric precursor synthesis. *Phys. Chem. Chem. Phys.* **2020**, *22*, 18868−18881.

(15) Gao, J.; et al. Breaking Long-Range Order in Iridium Oxide by Alkali Ion for Efficient Water Oxidation. *J. Am. Chem. Soc.* **2019**, *141*, 3014−3023.

(16) Willinger, E.; Massué, C.; Schlögl, R.; Willinger, M. G. Identifying Key Structural Features of IrO_x Water Splitting Catalysts. *J. Am. Chem. Soc.* **2017**, *139*, 12093−12101.

(17) Sun, W.; Song, Y.; Gong, X.-Q.; Cao, L.-M.; Yang, J. Hollandite Structure $Kx_{\approx 0.25}IrO_2$ Catalyst with Highly Efficient Oxygen Evolution Reaction. *ACS Appl. Mater. Interfaces* **2016**, *8*, 820−826.

(18) Ruiz Esquius, J.; Morgan, D. J.; Spanos, I.; Hewes, D. G.; Freakley, S. J.; Hutchings, G. J. Effect of Base on the Facile Hydrothermal Preparation of Highly Active IrO_x Oxygen Evolution Catalysts. *ACS Appl. Energy Mater.* **2020**, *3*, 800−809.

(19) Shi, L. et al. in *Materials Processing Fundamentals*. (eds Lee, J. et al.); (Springer International Publishing), 2020, 107−116.

(20) Tsirlin, A. A.; Gegenwart, P. Kitaev Magnetism through the Prism of Lithium Iridate. *Phys. Status Solidi B Basic Res.* **2022**, *259*, No. 2100146.

(21) Freund, F.; et al. Single crystal growth from separated educts and its application to lithium transition-metal oxides. *Sci. Rep.* **2016**, *6*, 35362.

(22) O'Malley, M. J.; Verweij, H.; Woodward, P. M. Structure and properties of ordered Li_2IrO_3 and Li_2PtO_3. *J. Solid State Chem.* **2008**, *181*, 1803−1809.

(23) Yang, C.; et al. Cation insertion to break the activity/stability relationship for highly active oxygen evolution reaction catalyst. *Nat. Commun.* **2020**, *11*, 1378.

(24) Li, L.; et al. Probing Electrochemically Induced Structural Evolution and Oxygen Redox Reactions in Layered Lithium Iridate. *Chem. Mater.* **2019**, *31*, 4341−4352.

(25) Pearce, P. E.; et al. Revealing the Reactivity of the Iridium Trioxide Intermediate for the Oxygen Evolution Reaction in Acidic Media. *Chem. Mater.* **2019**, *31*, 5845−5855.

(26) Kobayashi, H.; Tabuchi, M.; Shikano, M.; Kageyama, H.; Kanno, R. Structure, and magnetic and electrochemical properties of layered oxides, Li_2IrO_3. *J. Mater. Chem.* **2003**, *13*, 957−962.

(27) Sanchez Casalongue, H. G.; et al. In Situ Observation of Surface Species on Iridium Oxide Nanoparticles during the Oxygen Evolution Reaction. *Angew. Chem., Int. Ed.* **2014**, *53*, 7169−7172.

(28) Velasco-Vélez, J.-J.; et al. Surface Electron-Hole Rich Species Active in the Electrocatalytic Water Oxidation. *J. Am. Chem. Soc.* **2021**, *143*, 12524−12534.

(29) Tsai, H. M.; et al. Comparison of electronic structures of RuO_2 and IrO_2 nanorods investigated by x-ray absorption and scanning photoelectron microscopy. *Appl. Phys. Lett.* **2007**, *90*, No. 042108.

(30) House, R. A.; et al. Covalency does not suppress O_2 formation in 4d and 5d Li-rich O-redox cathodes. *Nat. Commun.* **2021**, *12*, 2975.

(31) Chen, J. G. NEXAFS investigations on transition metal oxide, nitrides, carbides, sulfides and other interstitial compounds. *Surf. Sci. Rep.* **1997**, *30*, 1−152.

(32) Romanov, D. P.; Skrobot, V. N. Distortions of Octahedra in Rutile-Type Structures of Transition Element Dioxides. *Glass Phys. Chem.* **2009**, *35*, 518−524.

(33) Nattino, F.; Marzari, N. Operando XANES from first-principles and its application to iridium oxide. *Phys. Chem. Chem. Phys.* **2020**, *22*, 10807−10818.

(34) Cruz, A. M.; et al. Iridium Oxohydroxide, a Significant Member in the Family of Iridium Oxides. Stoichiometry, Characterization, and

Implications in Bioelectrodes. *J. Phys. Chem. C* **2012**, *116*, 5155−5168.
(35) Oakton, E.; et al. IrO_2-TiO_2: A High-Surface-Area, Active, and Stable Electrocatalyst for the Oxygen Evolution Reaction. *ACS Catal.* **2017**, *7*, 2346−2352.
(36) McCalla, E.; et al. Visualization of O-O peroxo-like dimers in high-capacity layered oxides for Li-ion batteries. *Science* **2015**, *350*, 1516−1521.
(37) Grimaud, A.; Hong, W. T.; Shao-Horn, Y.; Tarascon, J. M. Anionic redox processes for electrochemical devices. *Nat. Mater.* **2016**, *15*, 121−126.
(38) Spanos, I.; et al. Standardized Benchmarking of Water Splitting Catalysts in a Combined Electrochemical Flow Cell/Inductively Coupled Plasma−Optical Emission Spectrometry (ICP-OES) Setup. *ACS Catal.* **2017**, *7*, 3768−3778.
(39) Fierro, S.; Kapałka, A.; Comninellis, C. Electrochemical comparison between IrO_2 prepared by thermal treatment of iridium metal and IrO_2 prepared by thermal decomposition of H_2IrCl_6 solution. *Electrochem. Commun.* **2010**, *12*, 172−174.
(40) Abbott, D. F.; et al. Iridium Oxide for the Oxygen Evolution Reaction: Correlation between Particle Size, Morphology, and the Surface Hydroxo Layer from Operando XAS. *Chem. Mater.* **2016**, *28*, 6591−6604.
(41) Diaz-Morales, O.; et al. Iridium-based double perovskites for efficient water oxidation in acid media. *Nat. Commun.* **2016**, *7*, 12363.
(42) Gottesfeld, S.; Srinivasan, S. Electrochemical and optical studies of thick oxide layers on iridium and their electrocatalytic activities for the oxygen evolution reaction. *J. Electroanal. Chem. Interfacial Electrochem.* **1978**, *86*, 89−104.
(43) Perez, A. J.; Beer, R.; Lin, Z.; Salager, E.; Taberna, P. L.; Abakumov, A. M.; Simon, P.; Tarascon, J. M. Proton Ion Exchange Reaction in Li_3IrO_4: A Way to New H_3+xIrO_4 Phases Electrochemically Active in Both Aqueous and Nonaqueous Electrolytes. *Adv. Energy Mater.* **2018**, *8*, No. 1702855.
(44) Lee, Y.; Suntivich, J.; May, K. J.; Perry, E. E.; Shao-Horn, Y. Synthesis and Activities of Rutile IrO_2 and RuO_2 Nanoparticles for Oxygen Evolution in Acid and Alkaline Solutions. *J. Phys. Chem. Lett.* **2012**, *3*, 399−404.
(45) Czioska, S.; et al. Increased Ir−Ir Interaction in Iridium Oxide during the Oxygen Evolution Reaction at High Potentials Probed by Operando Spectroscopy. *ACS Catal.* **2021**, *11*, 10043−10057.
(46) Povia, M.; Abbott, D. F.; Herranz, J.; Heinritz, A.; Lebedev, D.; Kim, B. J.; Fabbri, E.; Patru, A.; Kohlbrecher, J.; Schäublin, R.; Nachtegaal, M.; Copéret, C.; Schmidt, T. J. Operando X-ray characterization of high surface area iridium oxides to decouple their activity losses for the oxygen evolution reaction. *Energy Environ. Sci.* **2019**, *12*, 3038−3052.
(47) Grimaud, A.; Demortière, A.; Saubanère, M.; Dachraoui, W.; Duchamp, M.; Doublet, M. L.; Tarascon, J. M. Activation of surface oxygen sites on an iridium-based model catalyst for the oxygen evolution reaction. *Nat. Energy* **2017**, *2*, 16189.
(48) Grimaud, A.; et al. Activating lattice oxygen redox reactions in metal oxides to catalyse oxygen evolution. *Nat. Chem.* **2017**, *9*, 457−465.
(49) Kasian, O.; Geiger, S.; Li, T.; Grote, J. P.; Schweinar, K.; Zhang, S.; Scheu, C.; Raabe, D.; Cherevko, S.; Gault, B.; Mayrhofer, K. J. J. Degradation of iridium oxides via oxygen evolution from the lattice: correlating atomic scale structure with reaction mechanisms. *Energy Environ. Sci.* **2019**, *12*, 3548−3555.
(50) Schweinar, K.; Gault, B.; Mouton, I.; Kasian, O. Lattice Oxygen Exchange in Rutile IrO_2 during the Oxygen Evolution Reaction. *J. Phys. Chem. Lett.* **2020**, *11*, 5008−5014.
(51) Streibel, V.; et al. Merging operando and computational X-ray spectroscopies to study the oxygen evolution reaction. *Curr. Opin. Electrochem.* **2022**, *35*, No. 101039.
(52) Massué, C.; et al. High-Performance Supported Iridium Oxohydroxide Water Oxidation Electrocatalysts. *ChemSusChem* **2017**, *10*, 1943−1957.
(53) Bernicke, M.; et al. Iridium Oxide Coatings with Templated Porosity as Highly Active Oxygen Evolution Catalysts: Structure-Activity Relationships. *ChemSusChem* **2015**, *8*, 1908−1915.
(54) Genovese, C.; et al. Operando spectroscopy study of the carbon dioxide electro-reduction by iron species on nitrogen-doped carbon. *Nat. Commun.* **2018**, *9*, 935.

https://doi.org/10.1021/jacs.2c13567
J. Am. Chem. Soc. 2023, 145, 6398−6409